nature physics

Article

https://doi.org/10.1038/s41567-024-02493-1

Single-component superconductivity in UTe_2 at ambient pressure

CONTENTS

DATA REPRODUCIBILITY

Figure 1 and Figure 2 show the relative change of elastic moduli as a function of temperature as obtained when different echoes from a single experiment are used for the data analysis. Figure 3 and Figure 4 show the relative change of elastic moduli for different carrier frequencies of the excited sound pulse. We find no significant dependence on either the echoes, or the frequencies used for any of our measurements.

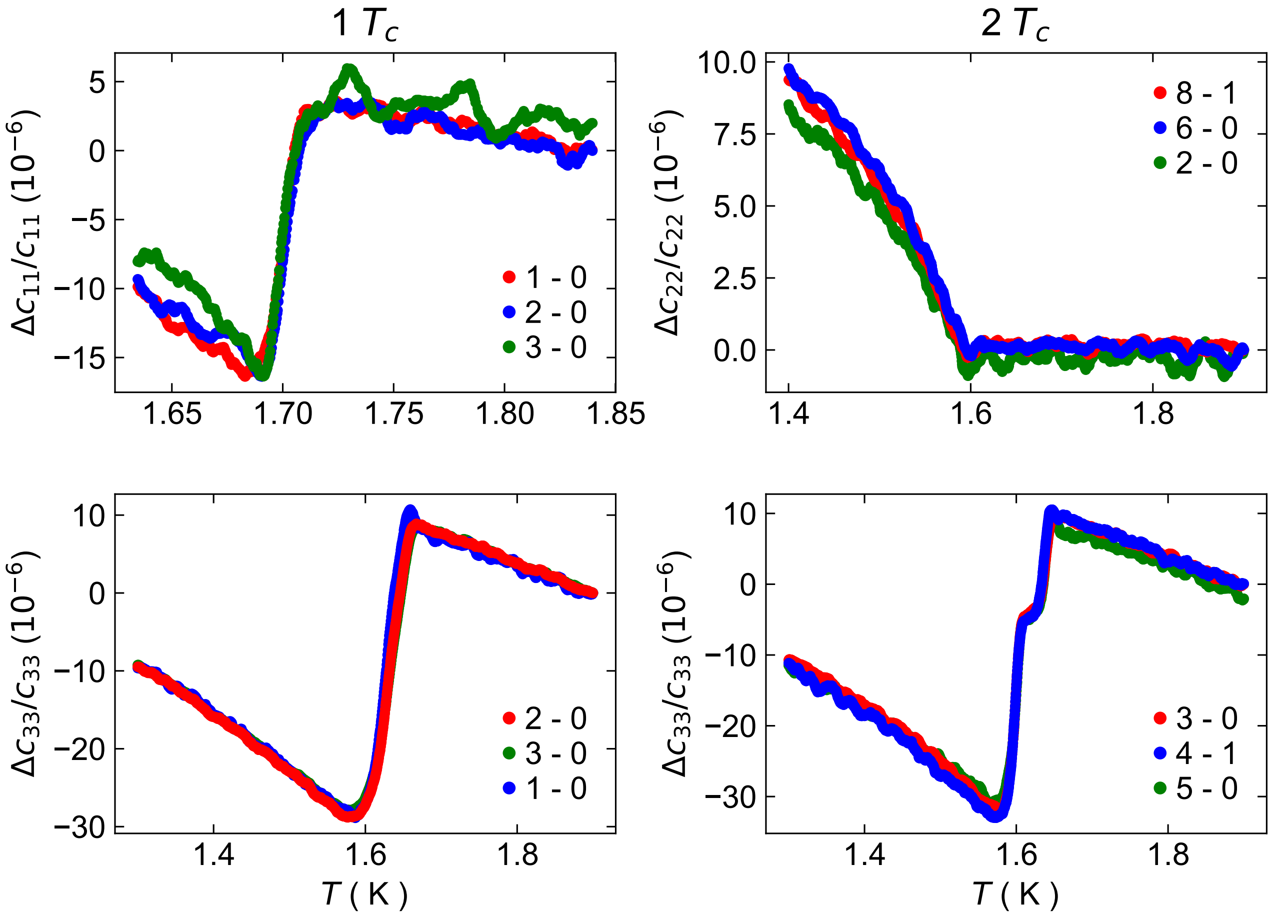

FIG. 1. **Echo Analysis Compressional Moduli.** The relative change of compressional elastic moduli as obtained from different echoes in a single pulse-echo ultrasound experiment. The colors indicate the echoes used for each curve. The data in red are the data shown in the main. The left column shows data for samples with one superconducting transition, the right column is for samples with two transitions.

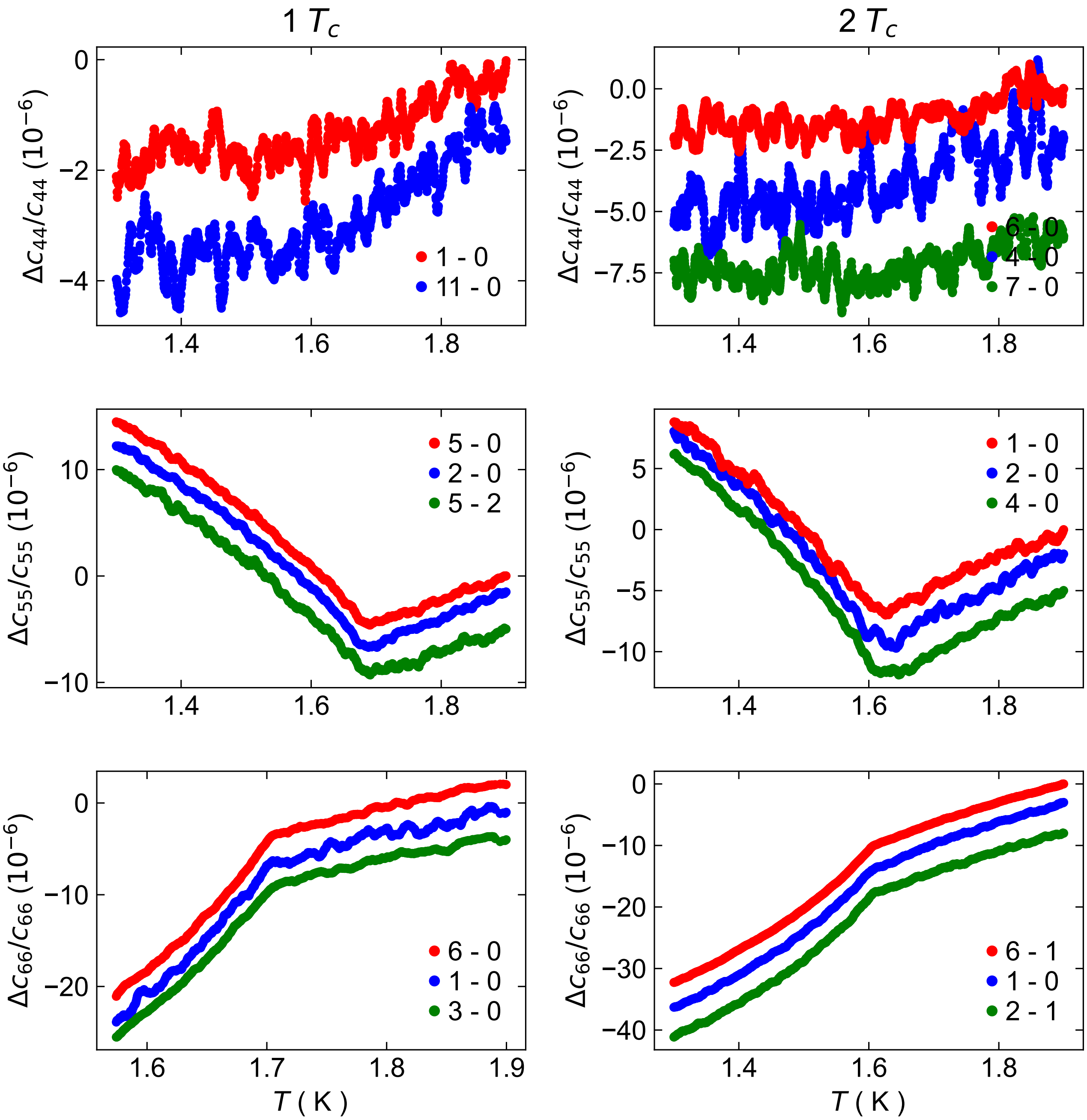

FIG. 2. **Echo Analysis Shear Moduli.** The relative change of shear elastic moduli as obtained from different echoes in a single pulse-echo ultrasound experiment. The colors indicate the echoes used for each curve. The data in red are the data shown in the main. The left column shows data for samples with one superconducting transition, the right column is for samples with two transitions.

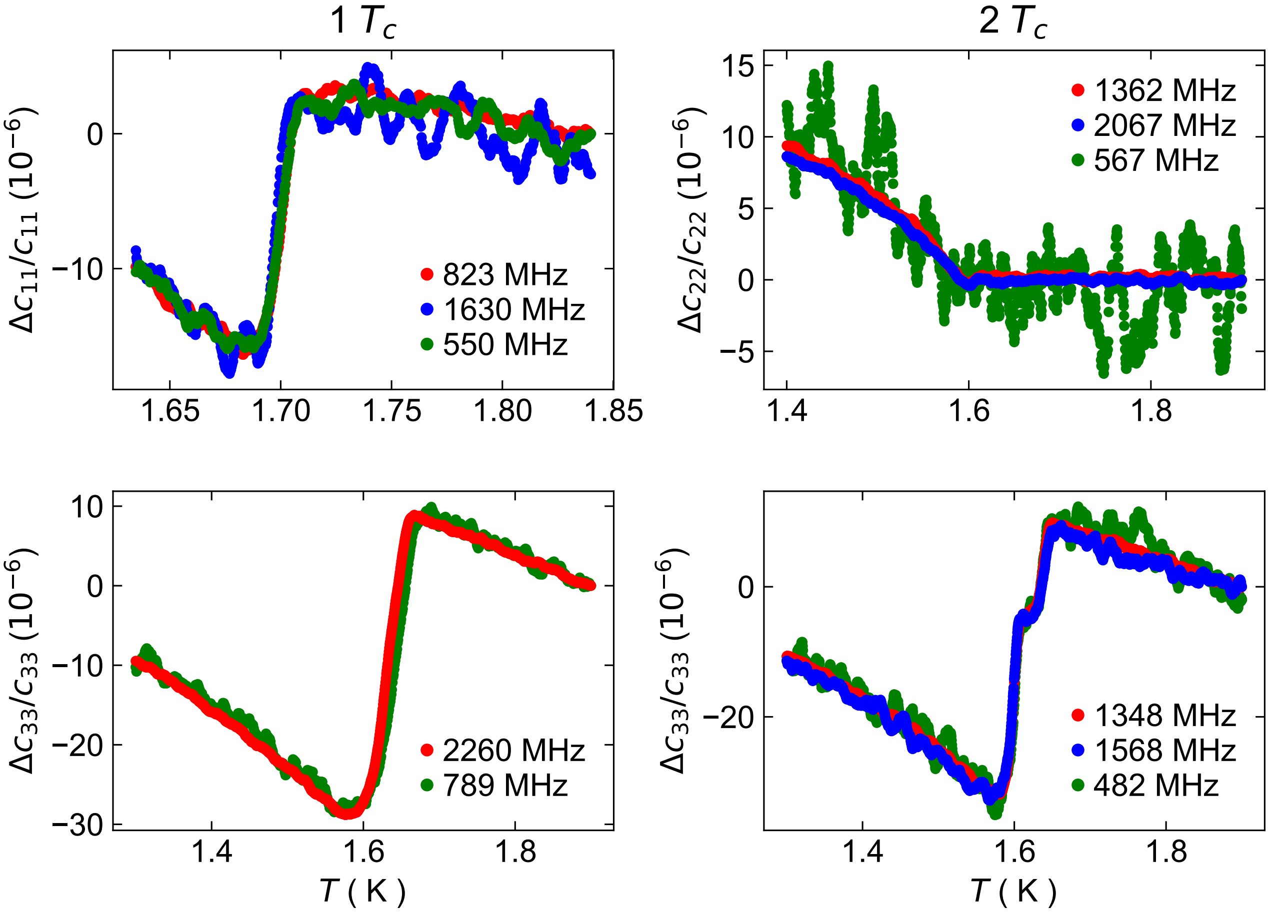

FIG. 3. **Frequency Dependence Compressional Moduli.** The relative change of compressional elastic moduli at different frequencies. The data in red are the data shown in the main. The left column shows data for samples with one superconducting transition, the right column is for samples with two transitions.

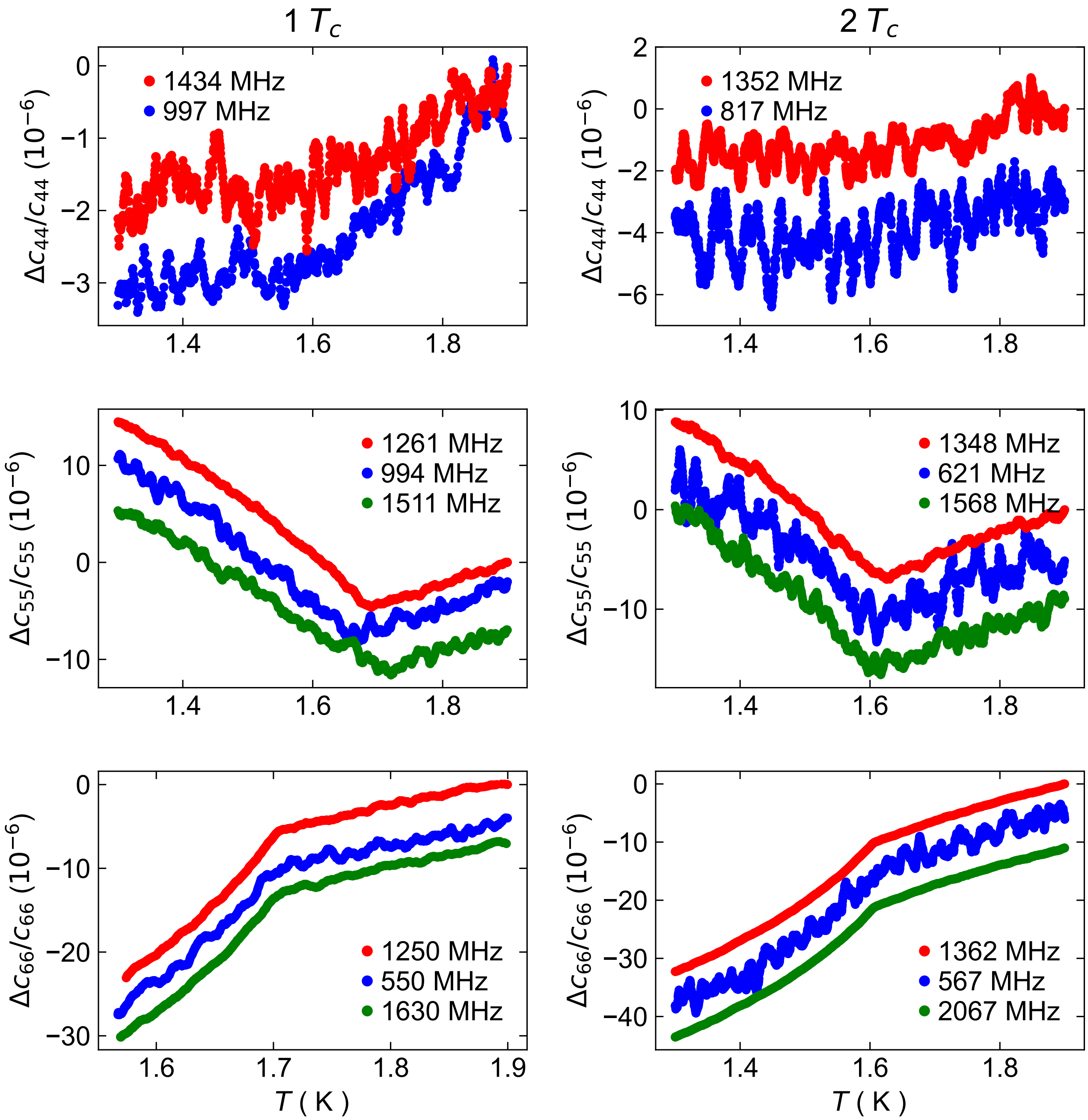

FIG. 4. **Frequency Dependence Shear Moduli.** The relative change of shear elastic moduli at different frequencies. The data in red are the data shown in the main. The left column shows data for samples with one superconducting transition, the right column is for samples with two transitions.

NOISE ANALYSIS

Figure 5 shows the relative change of all elastic moduli also shown in the main. In order to estimate the noise of our data, a second order polynomial has been fitted to the normal state data (highlighted by a red background in Figure 5). In Figure 6 we show the same elastic moduli with that polynomial subtracted from the data. We then estimate its noise as the RMS of the background-subtracted data above the transition, i.e. the same temperature range which we used to fit said polynomial background (red shaded region). The resulting RMS values lie between 0.04 ppm and 0.41 ppm (on average less than 1.9×10^{-7}).

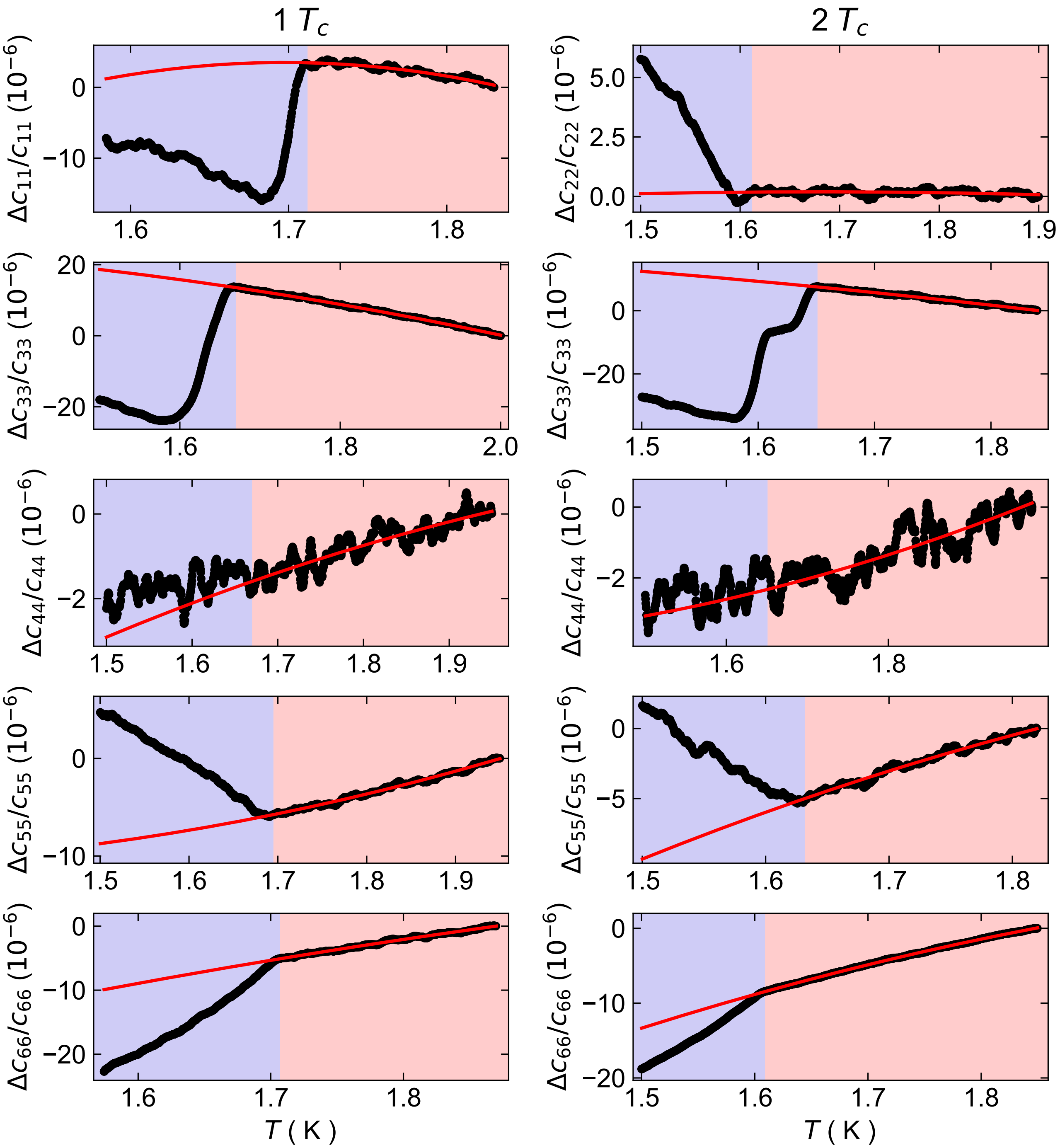

FIG. 5. **Background Subtraction.** Temperature dependence of all elastic moduli shown in the main (black points). A second order polynomial (red line) has been fitted to each modulus in the normal state above T_c (red shaded region). The left column shows data for samples with one superconducting transition, the right column is for samples with two transitions.

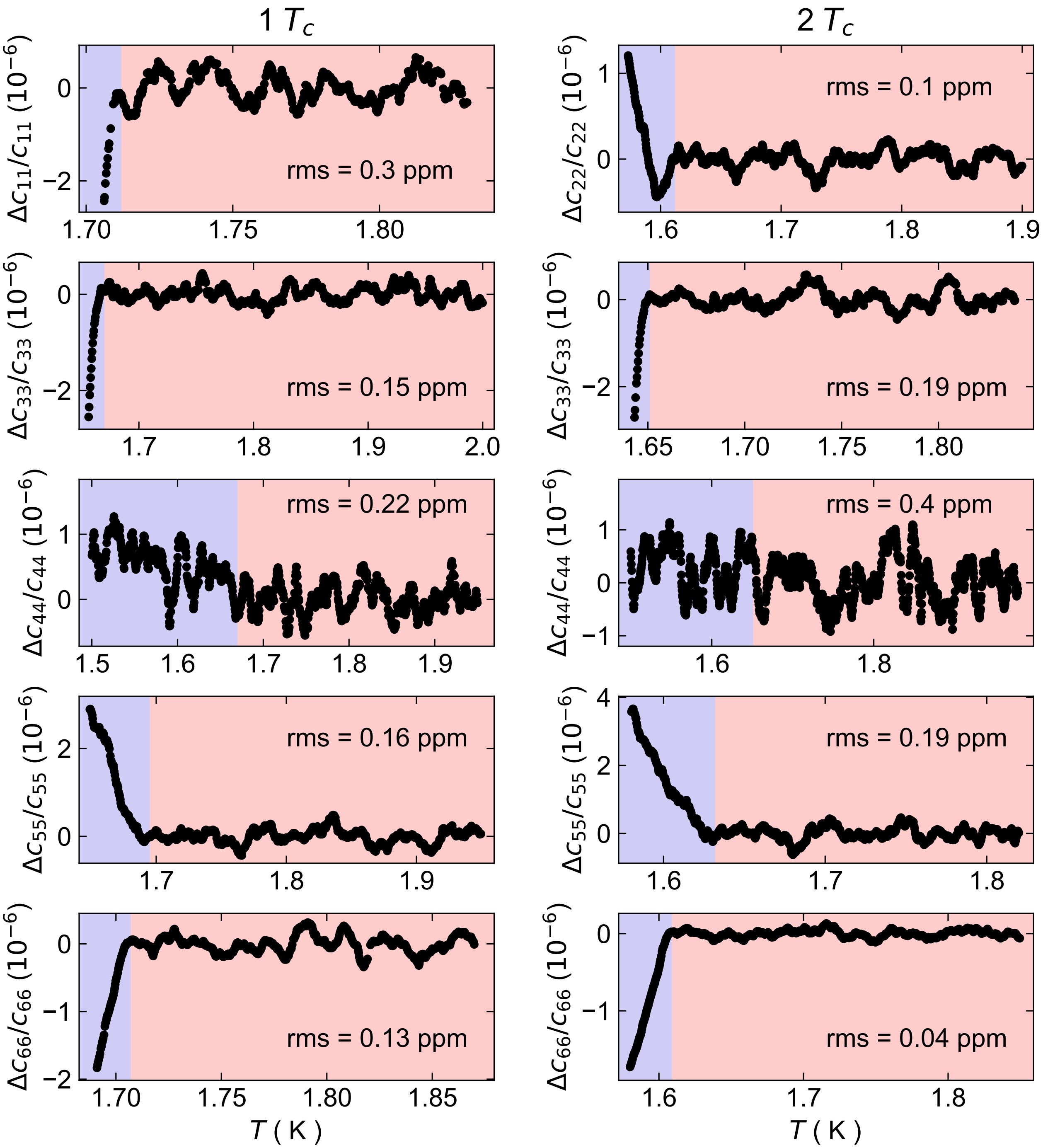

FIG. 6. **Noise Estimate.** Elastic moduli from Figure 5 with the normal state background (see Figure 5) subtracted. A RMS is calculated for each modulus in the same temperature range that was used to fit the background in Figure 5 (red shaded region). The purple/red shaded temperature regions are identical to those in Figure 5. The left column shows data for samples with one superconducting transition, the right column is for samples with two transitions.

LANDAU FREE ENERGY CALCULATIONS

Elastic moduli are the second derivative of the free energy with respect to strain, i.e. they are the strain susceptibility, in analogy with the heat capacity, which is the second derivative of the free energy with respect to temperature. If strain couples linearly to the square of the order parameter η (just like temperature does in the term $(T - T_c)\eta^2$), the respective elastic modulus will exhibit a discontinuity at the phase transition (just like the specific heat does). The reason for these discontinuities is that immediately below T_c, the system has a new degree of freedom that can respond when you apply strain (in the case of elastic moduli) or change temperature (in the case of heat capacity). This new degree of freedom means that the response below T_c is entirely distinct from that above T_c: even though the order parameter itself changes continuously, the system's susceptibility to changes in the order parameter is discontinuous.

For a single-component order parameter, only compressional moduli can exhibit this discontinuity. For a two-component order parameter, on the other hand, discontinuities in compressional moduli *and* certain shear moduli are allowed. This is because for single-component order parameters, the only quantity that can respond to strain is the magnitude of the order parameter. The bare "amplitude" of the order parameter breaks gauge symmetry and thus cannot enter directly into the free energy or couple linearly to external parameters like strain. As the magnitude of the order parameter is a scalar (simply a number), this means that it couples to scalar strains, i.e. compressional moduli.

For a two component order parameter, there are two new gauge-invariant quantities that can couple to strain: the relative phase between the components of the order parameter, and the overall "orientation" of the two components in order-parameter space. These are new degrees of freedom that can be probed by shear strain, and thus are what allow for discontinuities in the shear moduli at T_c.

Below, we elaborate on these concepts within the Landau theory of second-order phase transitions.

Elastic Free Energy

The elastic free energy of a solid is given by $\frac{1}{2}\sum_{i,j} \varepsilon_i c_{ij} \varepsilon_j$, with strain $\vec{\varepsilon} = \{\varepsilon_{xx}, \varepsilon_{yy}, \varepsilon_{zz}, 2\varepsilon_{yz}, 2\varepsilon_{xz}, 2\varepsilon_{xy}\}$ and the elastic tensor $\boldsymbol{c}$ in Voigt notation. In an orthorhombic crystal environment (i.e. point group D_{2h}), all individual elements of the strain tensor transform as a particular irreducible representation of the point group D_{2h}. In particular, we can rewrite

$$\vec{\varepsilon} = \{\varepsilon_{xx}, \varepsilon_{yy}, \varepsilon_{zz}, 2\varepsilon_{yz}, 2\varepsilon_{xz}, 2\varepsilon_{xy}\} = \{\varepsilon_{Ag,1}, \varepsilon_{Ag,2}, \varepsilon_{Ag,3}, \varepsilon_{B3g}, \varepsilon_{B2g}, \varepsilon_{B1g}\}, \tag{1}$$

where the subscript now refers to the irreducible representation. Consequently, the elastic free energy can be rewritten as

$$\begin{aligned} f_{el} =& \frac{1}{2}\left(c_{Ag,1}\varepsilon_{Ag,1}^2 + c_{Ag,2}\varepsilon_{Ag,2}^2 + c_{Ag,3}\varepsilon_{Ag,3}^2 + 2c_{Ag,4}\varepsilon_{Ag,1}\varepsilon_{Ag,2} + 2c_{Ag,5}\varepsilon_{Ag,1}\varepsilon_{Ag,3} + 2c_{Ag,6}\varepsilon_{Ag,2}\varepsilon_{Ag,3}\right. \\ & \left. + c_{B3g}\varepsilon_{B3g}^2 + c_{B2g}\varepsilon_{B2g}^2 + c_{B2g}\varepsilon_{B2g}^2\right). \end{aligned} \tag{2}$$

Here, we have rewritten the elastic tensor according to

$$\boldsymbol{c} = \begin{pmatrix} c_{11} & c_{12} & c_{13} & 0 & 0 & 0 \\ c_{12} & c_{22} & c_{23} & 0 & 0 & 0 \\ c_{13} & c_{23} & c_{33} & 0 & 0 & 0 \\ 0 & 0 & 0 & c_{44} & 0 & 0 \\ 0 & 0 & 0 & 0 & c_{55} & 0 \\ 0 & 0 & 0 & 0 & 0 & c_{66} \end{pmatrix} = \begin{pmatrix} c_{Ag,1} & c_{Ag,4} & c_{Ag,5} & 0 & 0 & 0 \\ c_{Ag,4} & c_{Ag,2} & c_{Ag,6} & 0 & 0 & 0 \\ c_{Ag,5} & c_{Ag,6} & c_{Ag,3} & 0 & 0 & 0 \\ 0 & 0 & 0 & c_{B3g} & 0 & 0 \\ 0 & 0 & 0 & 0 & c_{B2g} & 0 \\ 0 & 0 & 0 & 0 & 0 & c_{B1g} \end{pmatrix}. \tag{3}$$

Order Parameter Free Energy and Coupling to Strain:
One-Component Order Parameter

A single-component superconducting order parameter (OP) can be parametrized as $\eta e^{i\gamma}$, with an amplitude η and phase γ, both real. However, since the free energy needs to obey global gauge symmetry, the OP can only appear in even powers and the phase factor $e^{i\gamma}$ becomes unobservable. Only one degree of freedom remains, the amplitude (or superfluid density) η. The phase factor is thus dropped in the following discussion. In this case, the OP free energy expansion to fourth order reads

$$f_{OP} = \frac{a}{2}\eta^2 + \frac{b}{4}\eta^4, \tag{4}$$

	One-Component OP $\eta_0 = \sqrt{\frac{-a}{b}}$	$B_{2u} + iB_{3u}$ $(\theta_0, \gamma_0) = (\pi/4, \pm\pi/2)$ $\eta_0 = \pm\sqrt{\frac{-2a_1}{b_1+b_3-b_4}}$
$\delta c_{Ag,i}$	$-\frac{g_i^2}{2b}\,(\eta)$	$\frac{a_1(-2a_2(b_1+b_3-b_4)g_i^a g_i^s + a_1(-(b_1+b_3-b_4)(g_i^a)^2 + 4b_2 g_i^a g_i^s - (b_1-b_3+b_4)(g_i^s)^2))}{a_1^2(b_1^2-4b_2^2-(b_3-b_4)^2)+4a_1a_2b_2(b_1+b_3-b_4)-a_2^2(b_1+b_3-b_4)^2}\,(\eta,\theta)$
δc_{B1g}	0	$-\frac{g_4^2}{2b_4}\,(\gamma)$
δc_{B2g}	0	0
δc_{B3g}	0	0

TABLE I. **Discontinuities in elastic moduli for different OP configurations.** Magnitudes of discontinuities in elastic moduli at T_c for one and two-component OPs, along with the particular degree of freedom that causes the discontinuity (given in parentheses after the expression for the discontinuity). For a one-component OP, only compressional moduli $c_{A_g,i}$ show a discontinuity, caused by fluctuations in the order parameter amplitude η. For a $B_{2u} + iB_{3u}$ two-component OP, compressional moduli and the c_{B1g} elastic modulus are allowed to show a discontinuity. The discontinuity in the compressional moduli is due to fluctuations in the absolute amplitdue η of the OP, as well as fluctuations in the relative amplitude θ between individual components. The discontinuity in c_{B1g}, however, is caused by fluctuations of the relative phase γ between different order parameter components.

where $a = a_0\,(T - T_c)$. $a_0 > 0$, and b are phenomenological constants, T_c is the critical temperature.

Since the OP has to appear in even powers in the free energy, the lowest possible coupling to strain is quadratic in OP and linear in strain. Furthermore, since the OP transforms as a one-dimensional irreducible representation of D_{2h}, its bilinear will always transform as the A_g irreducible representation, irrespective of the particular representation. Thus, quadratic in OP and linear in strain coupling terms are only allowed for A_g strains, and to lowest order, the terms in the free energy coupling the OP to strain are

$$f_{coupling} = \frac{1}{2}\left(g_1\varepsilon_{Ag,1} + g_2\varepsilon_{Ag,2} + g_3\varepsilon_{Ag,3}\right)\eta^2. \tag{5}$$

Following the formalism outlined in [1], coupling of strain to the OP leads to a discontinuity of the respective elastic moduli at T_c according to

$$\delta c_{mn} = -\left.\frac{Z_m Z_n}{Y}\right|_{\eta\to\eta_0,\varepsilon_m\to 0}, \tag{6}$$

where $Z_m = \frac{\partial^2 f_{coupling}}{\partial\eta\partial\varepsilon_m}$, $Y = \frac{\partial^2 f_{OP}}{\partial\eta^2}$, and $\eta_0 = \sqrt{\frac{-a}{b}}$ is the equilibrium value for the OP defined by $\partial f_{OP}/\partial\eta = 0$. From Equation 6 it is straightforward to see that coupling terms in the free energy which are quadratic or higher order in strain will not lead to a discontinuity of the respective elastic modulus at T_c, which justifies the truncation of Equation 5 after terms linear in strain. Consequently, in the case of a one-component OP, no shear modulus (i.e. c_{B1g}, c_{B2g}, or c_{B3g}) is allowed to show a discontinuity at T_c (note that a discontinuity in its derivative is allowed [2]). This is a general statement purely based on the dimensionality of the order parameter and irrespective of its particular irreducible representation. Combining Equation 5 and Equation 6, all A_g elastic moduli exhibit a discontinuity at the critical temperature. The magnitudes of these discontinuities based on the free energy in Equation 4 and Equation 5 are summarized in Table I.

Order Parameter Free Energy and Coupling to Strain:
Two-Component Order Parameter

Next we discuss discontinuities in the elastic moduli with a two-component OP $\boldsymbol{\eta} = \{\eta_x, \eta_y\}$. In the D_{2h} point group, all irreducible representations are one dimensional. A two-component order parameter therefore has to consist of two one-component order parameters, meaning η_x and η_y can belong to different irreducible representations and are not related by symmetry. The example of η_x and η_y transforming as the B_{2u} and B_{3u} irreducible representations, respectively, as suggested for the superconducting OP in UTe$_2$ by authors in Hayes *et al.* [3] and Wei *et al.* [4], will be used in the discussion below. For this particular OP, three independent bilinear combinations can be formed: $|\eta_x|^2$,

$|\eta_y|^2$, and $\left(\eta_x\eta_y^* + \eta_x^*\eta_y\right)$ transforming as A_g, A_g, and B_{1g} representations respectively. The Landau free energy reads

$$\begin{aligned} f_{OP} &= \frac{a_1}{2}\left(|\eta_x|^2 + |\eta_y|^2\right) + \frac{a_2}{2}\left(|\eta_x|^2 - |\eta_y|^2\right) \\ &+ \frac{b_1}{4}\left(|\eta_x|^4 + |\eta_y|^4\right) + \frac{b_2}{4}\left(|\eta_x|^4 - |\eta_y|^4\right) + \frac{b_3}{2}|\eta_x|^2|\eta_y|^2 + \frac{b_4}{4}\left(\left(\eta_x\eta_y^*\right)^2 + \left(\eta_x^*\eta_y\right)^2\right), \end{aligned} \tag{7}$$

where $a_{1,2} = a_{1,2}^{(0)}\left(T - T_c\right)$, $a_{1,2} > 0$, and b_i are phenomenological constants. Based on these considerations, the free energy coupling the OP to linear powers of strain can be written as

$$\begin{aligned} f_{coupling} &= \frac{1}{2}\left(g_1^s\varepsilon_{Ag,1} + g_2^s\varepsilon_{Ag,2} + g_3^s\varepsilon_{Ag,3}\right)\left(|\eta_x|^2 + |\eta_y|^2\right) + \frac{1}{2}\left(g_1^a\varepsilon_{Ag,1} + g_2^a\varepsilon_{Ag,2} + g_3^a\varepsilon_{Ag,3})\right]\left(|\eta_x|^2 - |\eta_y|^2\right) \\ &+ \frac{g_4}{2}\varepsilon_{B1g}\left(\eta_x\eta_y^* + \eta_x^*\eta_y\right). \end{aligned} \tag{8}$$

Coupling of B_{1g} strain to the second power of the OP as in the free energy above is only possible for the particular example of a $\{B_{2u}, B_{3u}\}$ OP. However, linear coupling of shear strain (i.e. B_{1g}, B_{2g}, or B_{3g} strain in D_{2h}) to a bilinear of the OP is in general only possible for a two-component OP.

In order to calculate the discontinuities of elastic moduli in the presence of a two-component OP, Ghosh *et al.* [1] generalized the expression in Equation 6 to

$$\delta c_{mn} = -\boldsymbol{Z}_m^T\boldsymbol{Y}^{-1}\boldsymbol{Z}_n\Big|_{\boldsymbol{\eta}\to\boldsymbol{\eta}_0,\varepsilon_m\to 0}, \tag{9}$$

where $\boldsymbol{Z}_m = \frac{\partial^2 f_{coupling}}{\partial\boldsymbol{\eta}\partial\varepsilon_m}$ and $\boldsymbol{Y} = \frac{\partial^2 f_{OP}}{\partial\boldsymbol{\eta}^2}$. Parametrizing the OP as $\boldsymbol{\eta} = \eta\left\{\cos\theta, e^{i\gamma}\sin\theta\right\}$, the derivative $\partial/\partial\boldsymbol{\eta}$ becomes $\partial/\partial\left\{\eta,\theta,\gamma\right\}$. Assuming a chiral order parameter $(\theta_0,\gamma_0) = (\pi/4, \pm\pi/2)$, the equilibrium amplitude η_0, defined by $\partial f_{OP}/\partial\eta|_{\eta_0,\theta_0,\gamma_0} = 0$, is then given by $\eta_0 = \pm\sqrt{\frac{-2a_1}{b_1+b_3-b_4}}$. This assumption is motivated by the observation of time-reversal symmetry breaking (TRSB) [3, 4] in the superconducting state of UTe$_2$. For this order parameter configuration, one finds

$$\boldsymbol{Y} = \begin{pmatrix} a_1 + \frac{3\eta_0^2}{2}\left(b_1 + b_3 - b_4\right) & -2\eta_0\left(a_2 + b_2\eta_0^2\right) & 0 \\ -2\eta_0\left(a_2 + b_2\eta_0^2\right) & \left(b_1 - b_3 + b_4\right)\eta_0^4 & 0 \\ 0 & 0 & \frac{b_4\eta_0^4}{2} \end{pmatrix}, \tag{10}$$

$$\boldsymbol{Z}_{Ag,i} = \begin{pmatrix} g_i^s\eta_0 \\ -g_i^a\eta_0^2 \\ 0 \end{pmatrix}, \quad \boldsymbol{Z}_{B1g} = \begin{pmatrix} 0 \\ 0 \\ -\frac{g_4\eta_0^2}{2} \end{pmatrix}, \quad \boldsymbol{Z}_{B2(3)g} = \begin{pmatrix} 0 \\ 0 \\ 0 \end{pmatrix}, \tag{11}$$

where $i = 1, 2, 3$. From Equation 10 and Equation 11 in can be seen that for a chiral $\{B_{2u}, B_{3u}\}$ order parameter in a D_{2h} point group, all compressional moduli (i.e. the elastic moduli corresponding to A_g strains) show a step discontinuity at T_c due to coupling of the corresponding strain to the absolute amplitude of the OP (the superfluid density), as well as the relative amplitude of the different components (this is in contrast to a multi-component OP where the different components are related by symmetry, for which compressional strains only couple to the absolute amplitude of the OP [1]). Among all the shear moduli, only c_{B1g} shows a step discontinuity at T_c, due to the coupling of B_{1g} shear strain to the relative phase between the different components of the OP.

While the details of the above calculation depend on the exact OP parameter configuration, the main statement is general: a multi-component OP is required for a discontinuity in any shear modulus.

HEAT CAPACITY MEASUREMENTS

Heat capacity measurements (Figure 7) were performed in a ^{3}He cryostat using the quasi-adiabatic method: a fixed power was applied to the calorimeter to raise it approximately 1% over the bath temperature. The power was then turned off to allow the calorimeter to relax back to the bath temperature. The heat capacity was extracted from these heating and cooling data by fitting them to exponentially-saturating curves. The sample was affixed to the calorimeter with Apiezon N grease. The background heat capacity of the grease and the calorimeter were measured separately and subtracted from the data in Figure 7.

EHRENFEST ANALYSIS

The discontinuity observed in the compressional moduli δc_{ii} at T_c is directly related to the jump in the heat capacity divided by temperature, $\Delta C/T$, via Ehrenfest relations. For a single component order parameter they read

$$\delta c_{ii} = -\frac{\Delta C}{T}\left(\frac{dT_c}{d\varepsilon_{ii}}\right)^2 . \tag{12}$$

The derivative of critical temperature with respect to compressional strain $dT_c/d\varepsilon_{ii}$ can therefore be calculated by extracting the discontinuities of the corresponding elastic modulus and the heat capacity at T_c. The heat capacity was measured in sample S3 (see Figure 7) and the size of its discontinuity at T_c is determined to be (196 ± 18) mJ/(mol K^2). The magnitudes of the discontinuities in $\Delta c/c$ for all compressional moduli are extracted according to Figure 8 and the values are given in Table II. Using these values, as well as the elastic moduli of UTe$_2$ [5], the absolute values of $dT_c/d\varepsilon_{ii}$ $(ii = xx, yy, zz)$ are calculated (see Table II).

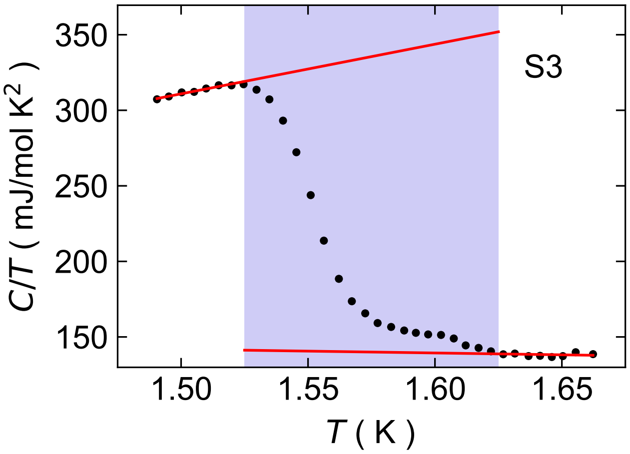

FIG. 7. **Heat Capacity.** Heat capacity divided by temperature as a function of temperature measured on sample S3. The jump at T_c is (196 ± 18) mJ/(mol K^2), determined according to linear fits below and above the transition (red lines). The uncertainty is estimated from the finite temperature range close to T_c in which the data deviates significantly from these fits. This range is indicated by the blue shaded region.

The derivatives of the critical temperature with respect to stress can be calculated from the derivatives with respect to strain via

$$\begin{pmatrix} dT_c/d\sigma_{xx} \\ dT_c/d\sigma_{yy} \\ dT_c/d\sigma_{zz} \end{pmatrix} = \begin{pmatrix} c11 & c12 & c13 \\ c12 & c22 & c23 \\ c13 & c23 & c33 \end{pmatrix}^{-1} \begin{pmatrix} dT_c/d\varepsilon_{xx} \\ dT_c/d\varepsilon_{yy} \\ dT_c/d\varepsilon_{zz} \end{pmatrix} . \tag{13}$$

The resulting values are given in Table II, along with values measured in uniaxial stress experiments [6]. The elastic tensor used for this calculation is again taken from Theuss *et al.* [5]. Note that the analysis in Equation 13 requires knowledge about the signs of $dT_c/d\varepsilon_{ii}$, whereas the Ehrenfest relations in Equation 12 only yield their absolute values. For a correct analysis from our data, signs according to Girod *et al.* [6] were assumed.

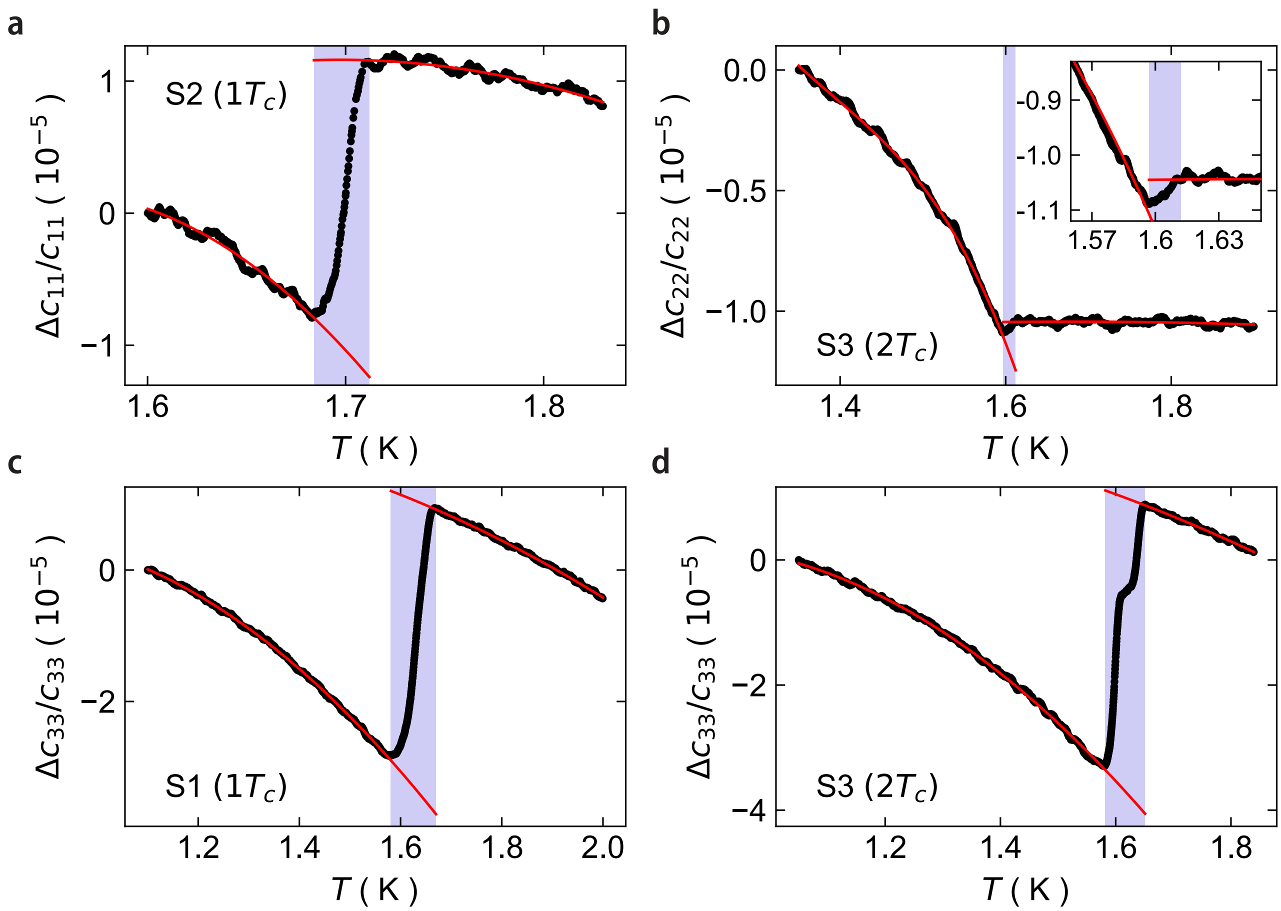

FIG. 8. **Step Discontinuities in Compressional Moduli.** Relative changes in compressional moduli across T_c (black points). The magnitude of the step discontinuity in compressional moduli is defined as the difference between polynomial fits to the data above and below T_c (red lines). The uncertainty is estimated from the finite temperature range close to T_c in which the data deviates significantly from these fits (indicated in blue). Extracted values are given in Table II. The elastic moduli shown are c_{11} (panel a) and c_{33} (panel c) for samples with one transition and c_{22} (panel b) and c_{33} (panel d) for samples with two transitions. The inset of panel b shows the relative change in c_{22} close to T_c.

Elastic Modulus	Step in $\frac{\Delta c}{c}$	$\frac{dT_c}{d\varepsilon_{ii}}$ $\left(\frac{\mathrm{K}}{\%\,\mathrm{strain}}\right)$	$\frac{dT_c}{d\sigma_{ii}}$ $\left(\frac{\mathrm{K}}{\mathrm{GPa}}\right)$	$\frac{dT_c}{d\sigma_{ii}}$ $\left(\frac{\mathrm{K}}{\mathrm{GPa}}\right)$ from [6]
c_{11} ($1T_c$)	$-(2.2 \pm 0.2) \times 10^{-5}$	-0.23 ± 0.02	-0.50 ± 0.03	-0.87
c_{22} ($2T_c$)	$-(0.13 \pm 0.07) \times 10^{-5}$	-0.07 ± 0.02	-0.09 ± 0.02	—
c_{33} ($1T_c$)	$-(4.4 \pm 0.3) \times 10^{-5}$	0.34 ± 0.02	0.60 ± 0.03	0.56
c_{33} ($2T_c$)	$-(4.7 \pm 0.2) \times 10^{-5}$	0.35 ± 0.02	0.62 ± 0.03	0.56

TABLE II. **Ehrenfest Analysis.** Derivatives of the critical temperature with respect to strain $dT_c/d\varepsilon$ are calculated based on the magnitudes of the discontinuities in $\Delta c/c$ extracted according to Figure 8. Values of the absolute elastic moduli and respective uncertainties are taken from Theuss *et al.* [5] and the size of the specific heat jump (or more precisely $\Delta C/T$) is taken to be 196 ± 18 mJ/(mol K^2) from Figure 7. Knowledge of the signs of $dT_c/d\varepsilon$ is required for the correct calculation of $dT_c/d\sigma$. Since 12 only yields their absolute value, the signs are chosen according to uniaxial stress experiments [6]. The last column shows a comparison to values from said uniaxial stress experiments in Girod *et al.* [6].

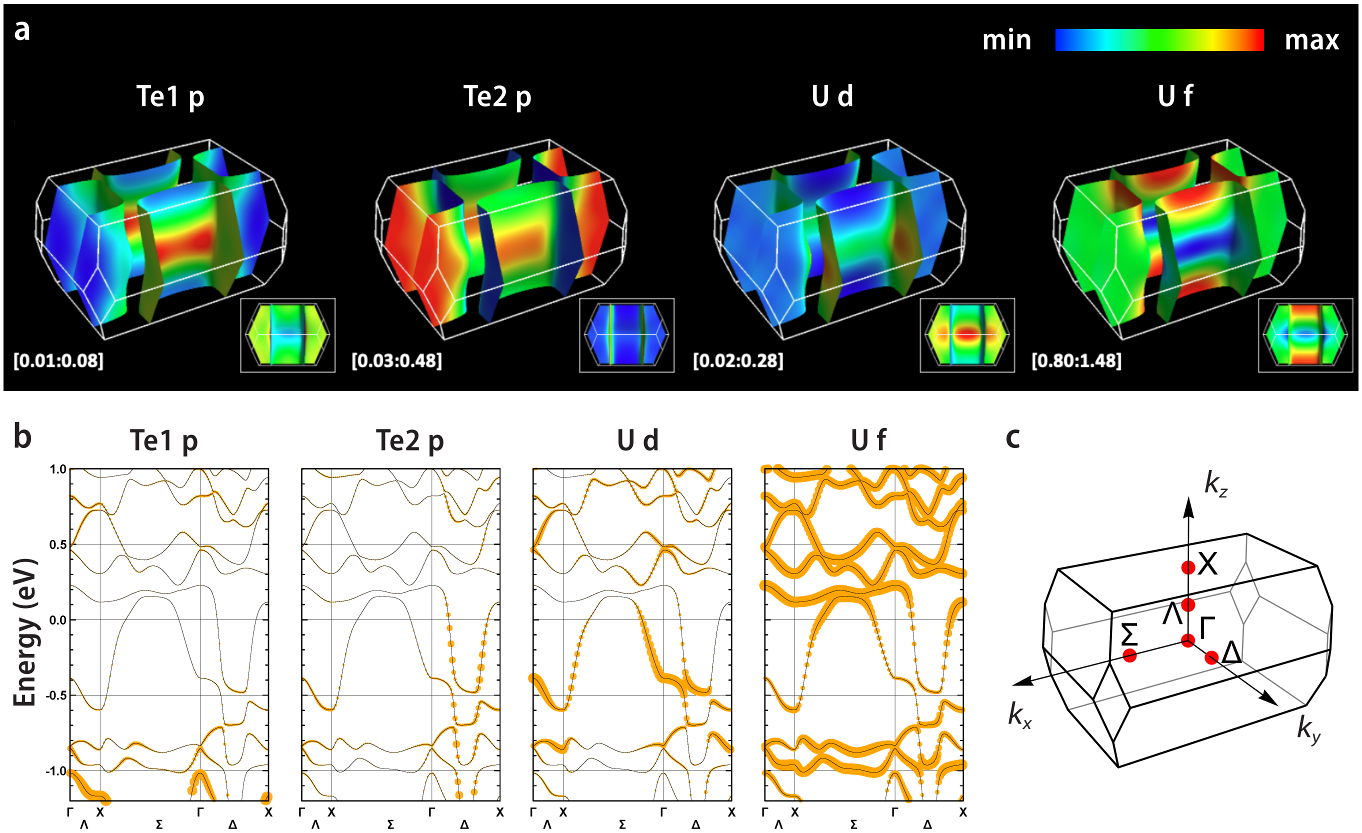

FIG. 9. **DFT Fermi Surface and Band Structure.** (a) Fermi surface of UTe_2 calculated with $U = 2$ eV. Fermi surfaces are colored according to their orbital Te1 p, Te2 p, U d, and U f content, from left to right, respectively. Color scales are rescaled between each plot, but respective minimum and maximum values are given to the bottom left of each panel. (b) Band structure calculated with the same parameters as in (a). Orange circles are sized according to the orbital weight of Te1 p, Te2 p, U d, and U f (from left to right) on each individual band. (c) UTe_2 Brillouin zone.

UTE$_2$ FERMI SURFACE AND SUPERCONDUCTING GAP

Density Functional Theory

Density-functional theory calculations are used to examine the orbital character of the electronic states in the vicinity of the chemical potential. The self-consistent field calculation is performed in the same way as in Theuss *et al.* [5], by additionally considering the Hubbard U for the uranium $5f$ electrons. The full-potential linearized augmented plane wave method [7] calculations employed the generalized gradient approximation [8] for the exchange correlation, wave function and potential energy cutffs of 16 and 200 Ry, respectively, and muffin-tin sphere radii of 1.35 Å. Spin-orbit coupling was fully taken into account in the assumed nonmagnetic state. We set $U = 2$ eV to obtain a quasi 2D Fermi surface [9, 10], which qualitatively accounts for the recent experiments. Along the high-symmetry lines in the Brillouin zone (Λ, Σ, and Δ lines, see Figure 9c) and on a dense $50\times50\times50$ k-point mesh, the (Kramers degenerate) band energy and wave functions are generated, and the orbital components of each doublet are calculated within the atom-centered spheres of radius 1.35 Å. In Figure 9, the orbital components are shown on the Fermi surface (panel a—the visualization of the Fermi surface is done with `FermiSurfer` [11]) and along the band dispersion (panel b).

Tight Binding Model

Figure 9 motivates a tight binding model constructed from two quasi-one-dimensional chain Fermi surfaces: one chain from the Te(2) $5p$ orbitals, and one from the U $6d$ orbitals. This model faithfully captures the shape of the Fermi surface measured by quantum oscillations (see [12]). This Fermi surface is quite similar to that calculated for $ThTe_2$,

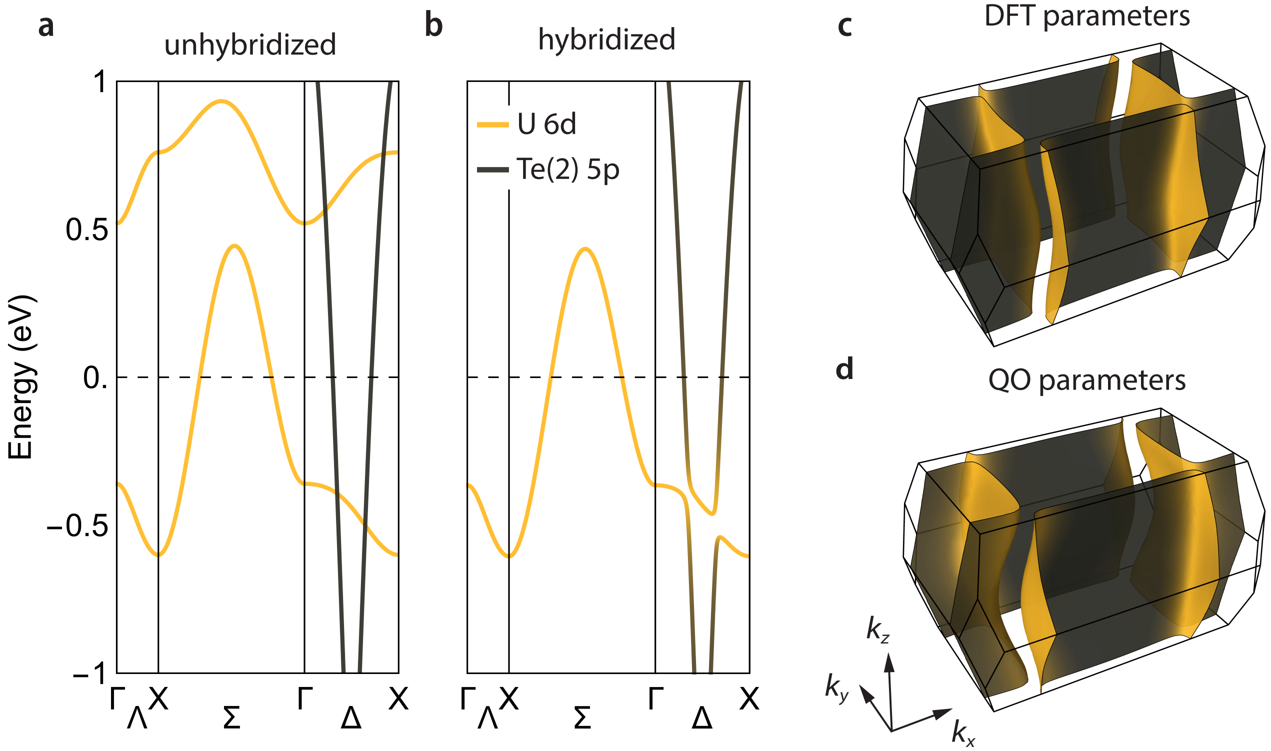

FIG. 10. **Tight Binding Model.** (a-c) Tight binding model with parameters to match DFT results. (a) Unhybridized bands formed by uranium 6*d* (yellow) and tellurium (2) 5*p* (gray) electrons. Bands crossing the Fermi level are hybridized in (b) and the resulting Fermi surface is shown in (c). Colors represent a projection on original U/Te(2) bands. (d) Fermi surface from tight binding model with parameters to match quantum oscillation results [12].

which has no f electrons—while the f electrons in UTe$_2$ hybridize strongly with both bands, the predominant effect is to enhance the cyclotron masses and shift the chemical potential, without strongly modifying the Fermi surface shape.

There are two uranium atoms that form a dimer in the center of the conventional unit cell shown in Figure 5a of the main text. The dominant tight binding parameters will be the chemical potential μ_U, the intra-dimer overlap Δ_U, the hopping t_U along the uranium chain in the a direction, the hopping t'_U to other uranium in the dimer along the chain direction, the hoppings $t_{ch,\mathrm{U}}$ and $t'_{ch,\mathrm{U}}$ between chains in the $a-b$ plane, and the hopping $t_{z,\mathrm{U}}$ between chains along the c axis. The two bands from the two uranium sites then come from diagonalizing the following matrix:

$$E_\mathrm{U} = \begin{bmatrix} \mu_\mathrm{U} - 2t_\mathrm{U}\cos k_x a - 2t_{ch,\mathrm{U}}\cos k_y b & -\Delta_\mathrm{U} - 2t'_\mathrm{U}\cos k_x a - 2t'_{ch,\mathrm{U}}\cos k_y b - 4t_{z,\mathrm{U}}e^{-ik_z c/2}\cos k_x \frac{a}{2}\cos k_y \frac{b}{2} \\ -\Delta_\mathrm{U} - 2t'_\mathrm{U}\cos k_x a - 2t'_{ch,\mathrm{U}}\cos k_y b - 4t_{z,\mathrm{U}}e^{ik_z c/2}\cos k_x \frac{a}{2}\cos k_y \frac{b}{2} & \mu_\mathrm{U} - 2t_\mathrm{U}\cos k_x a - 2t_{ch,\mathrm{U}}\cos k_y b \end{bmatrix}. \tag{14}$$

There are in principle 4 Te(2) sites per conventional unit cell, but by including only nearest-neighbor hopping in the $a-b$ plane, the problem is again reduced to diagonalizing a 2×2 matrix. The dominant tight binding parameters are then the chemical potential μ_Te, the intra-unit-cell overlap Δ_Te between the two Te(2) atoms along the chain direction, the hopping t_Te along the Te(2) chain in the b direction, the hopping $t_{ch,\mathrm{Te}}$ between chains in the a direction, and the hopping $t_{z,\mathrm{Te}}$ between chains along the c axis. The tight binding matrix is:

$$E_\mathrm{Te} = \begin{bmatrix} \mu_\mathrm{Te} - 2t_{ch,\mathrm{Te}}\cos k_x a & -\Delta_\mathrm{Te} - t_\mathrm{te}e^{-ik_y b} - 2t_{z,\mathrm{Te}}\cos k_z \frac{c}{2}\cos k_x \frac{a}{2}\cos k_y \frac{b}{2} \\ -\Delta_\mathrm{Te} - t_\mathrm{te}e^{ik_y b} - 2t_{z,\mathrm{Te}}\cos k_z \frac{c}{2}\cos k_x \frac{a}{2}\cos k_y \frac{b}{2} & \mu_\mathrm{Te} - 2t_{ch,\mathrm{Te}}\cos k_x a \end{bmatrix}. \tag{15}$$

The resultant bands are plotted in Figure 10a. The tight binding parameters were chosen to roughly match the DFT result shown in Figure 9 and are given in Table III. The two bands crossing the Fermi energy can be hybridized to form the electron and hole pocket. We use an isotropic in momentum hybridization δ and chose its value to roughly match the DFT result. The resultant two bands that cross the Fermi energy are shown in Figure 10b, and the 3D Fermi surface is shown in Figure 10c. The predominant difference between the FS calculated with $U = 2$ eV and the FS reported by Eaton *et al.* [12] is that the latter was chosen with the opposite-sign dispersion along the c-axis. Tight binding parameters chosen to roughly match the FS reported in Eaton *et al.* [12] are also given in Table III, with the resultant FS shown in Figure 10d.

	$\Delta_{\rm U}$	$t_{\rm U}$	$t'_{\rm U}$	$t_{ch,{\rm U}}$	$t'_{ch,{\rm U}}$	$t_{z,{\rm U}}$	$\mu_{\rm Te}$	$\Delta_{\rm Te}$	$t_{\rm Te}$	$t_{ch,{\rm Te}}$	$t_{z,{\rm Te}}$	δ
DFT	0.40	0.15	0.08	0.01	0.00	-0.03	-1.80	-1.50	-1.50	0.00	-0.05	0.09
QO	0.05	0.10	0.08	0.01	0.00	0.04	-1.80	-1.50	-1.50	-0.03	-0.5	0.10

TABLE III. All parameters given in eV.

Superconducting Gap

When considering the symmetries of superconducting gaps, it is necessary to distinguish the cases of weak and strong spin-orbit coupling: UTe_2 likely falls in the latter category. However, since the orthorhombic point group of UTe_2 (D_{2h}) is inversion symmetric, one can still label irreducible representations as even or odd. This classification is used to distinguish spin singlet (even) or triplet (odd) superconductors. Since UTe_2 is most likely a spin-triplet superconductor, the possible irreducible representations of the order parameter are A_u, B_{1u}, B_{2u}, and B_{3u}. In the strong spin-orbit limit, they correspond to the following $\vec{d}$-vectors [13]

$$\vec{d}_{A_u} = \{\alpha k_x, \beta k_y, \gamma k_z\}\,, \tag{16}$$

$$\vec{d}_{B_{1u}} = \{\alpha k_y, \beta k_x, \gamma k_x k_y k_z\}\,, \tag{17}$$

$$\vec{d}_{B_{2u}} = \{\alpha k_z, \beta k_x k_y k_z, \gamma k_x\}\,, \tag{18}$$

$$\vec{d}_{B_{3u}} = \{\alpha k_x k_y k_z, \beta k_z, \gamma k_y\}\,, \tag{19}$$

where α, β, and γ are real constants and the momentum dependence of the superconducting gap is given by

$$\Delta\left(\vec{k}\right) = \sqrt{\vec{d}\cdot\vec{d}^{\star} \pm \left|\vec{d}\times\vec{d}^{\star}\right|}. \tag{20}$$

Here, $\vec{d}^{\star}$ is the complex conjugate of $\vec{d}$. The A_u order parameter is fully gapped, whereas the B_{1u}, B_{2u}, and B_{3u} order parameters have point nodes along the k_z, k_y, and k_x directions respectively. A B_{1u} gap is thus also fully gapped on the Fermi surface of UTe_2 found by quantum oscillations [12, 14] and only exhibits point nodes on a putative Fermi pocket enclosing the Γ-point [15].

The gap structures shown in the main text are calculated at $k_z = 0$ with $\alpha = \beta = \gamma$. A slight anisotropy in these parameters can change the exact shape of the momentum dependence of the different gap symmetries, but will not change their nodal structure.

Normal State Elastic Moduli

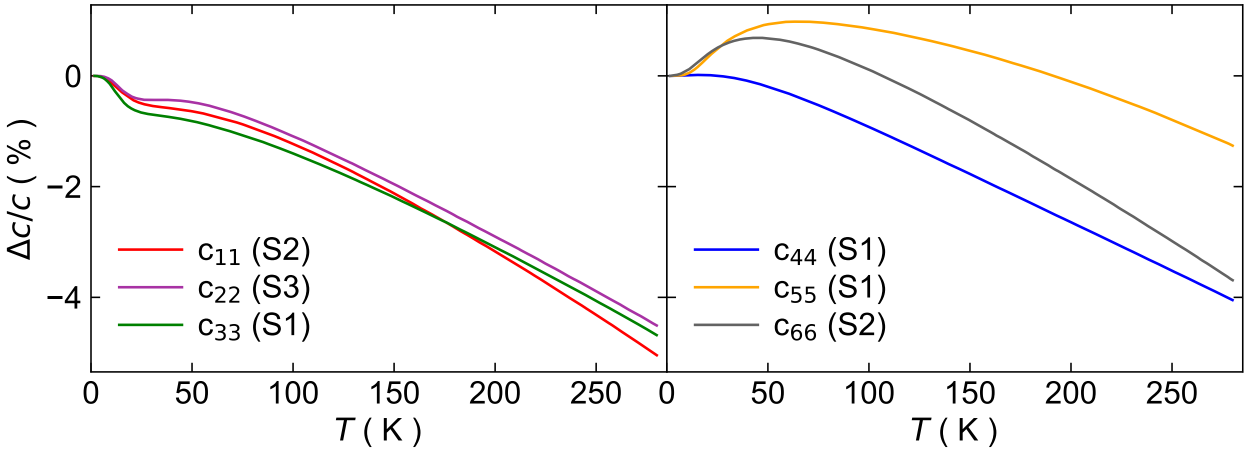

FIG. 11. **Normal State Elastic Moduli.** Relative changes of the normal state elastic moduli of UTe_2 from about 2 K to 280 K. Compressional moduli (c_{11}, c_{22}, c_{33}) and shear moduli (c_{44}, c_{55}, c_{66}) are shown in the left and right panels, respectively. The elastic moduli were measured at the following frequencies: 829 MHz (c_{11}), 1316 MHz (c_{22}), 1392 MHz (c_{33}), 1392 MHz (c_{44}), 1436 MHz (c_{55}), 829 MHz (c_{66}). Our measurements of c_{33}, c_{44}, and c_{55} agree with the data previously reported by Ushida *et al.* [16].

[1] S. Ghosh, A. Shekhter, F. Jerzembeck, N. Kikugawa, D. A. Sokolov, M. Brando, A. P. Mackenzie, C. W. Hicks, and B. J. Ramshaw, Thermodynamic evidence for a two-component superconducting order parameter in Sr_2RuO_4, Nature Physics **17**, 199 (2021).

[2] B. J. Ramshaw, A. Shekhter, R. D. McDonald, J. B. Betts, J. N. Mitchell, P. H. Tobash, C. H. Mielke, E. D. Bauer, and A. Migliori, Avoided valence transition in a plutonium superconductor, Proceedings of the National Academy of Sciences of the United States of America **112**, 3285 (2015).

[3] I. M. Hayes, D. S. Wei, T. Metz, J. Zhang, Y. S. Eo, S. Ran, S. R. Saha, J. Collini, N. P. Butch, D. F. Agterberg, A. Kapitulnik, and J. Paglione, Multicomponent superconducting order parameter in UTe_2, Science **373**, 797 (2021).

[4] D. S. Wei, D. Saykin, O. Y. Miller, S. Ran, S. R. Saha, D. F. Agterberg, J. Schmalian, N. P. Butch, J. Paglione, and A. Kapitulnik, Interplay between magnetism and superconductivity in UTe_2, Physical Review B **105**, 024521 (2022).

[5] F. Theuss, G. d. l. F. Simarro, A. Shragai, G. Grissonnanche, I. M. Hayes, S. Saha, T. Shishidou, T. Chen, S. Nakatsuji, S. Ran, M. Weinert, N. P. Butch, J. Paglione, and B. J. Ramshaw, Resonant ultrasound spectroscopy for irregularly shaped samples and its application to uranium ditelluride, Phys. Rev. Lett. **132**, 066003 (2024).

[6] C. Girod, C. R. Stevens, A. Huxley, E. D. Bauer, F. B. Santos, J. D. Thompson, R. M. Fernandes, J.-X. Zhu, F. Ronning, P. F. S. Rosa, and S. M. Thomas, Thermodynamic and electrical transport properties of UTe_2 under uniaxial stress, Physical Review B **106**, L121101 (2022).

[7] M. Weinert, G. Schneider, R. Podloucky, and J. Redinger, FLAPW: Applications and implementations, Journal of Physics: Condensed Matter **21**, 084201 (2009).

[8] J. P. Perdew, K. Burke, and M. Ernzerhof, Generalized Gradient Approximation Made Simple, Phys. Rev. Lett. **77**, 3865 (1996).

[9] J. Ishizuka, S. Sumita, A. Daido, and Y. Yanase, Insulator-metal transition and topological superconductivity in UTe_2 from a first-principles calculation, Physical Review Letters **123**, 217001 (2019).

[10] T. Shishidou, H. G. Suh, P. M. R. Brydon, M. Weinert, and D. F. Agterberg, Topological band and superconductivity in UTe_2, Physical Review B **103**, 104504 (2021).

[11] M. Kawamura, Fermisurfer: Fermi-surface viewer providing multiple representation schemes, Computer Physics Communications **239**, 197 (2019).

[12] A. G. Eaton, T. I. Weinberger, N. J. M. Popiel, Z. Wu, A. J. Hickey, A. Cabala, J. Pospíšil, J. Prokleška, T. Haidamak, G. Bastien, P. Opletal, H. Sakai, Y. Haga, R. Nowell, S. M. Benjamin, V. Sechovský, G. G. Lonzarich, F. M. Grosche, and M. Vališka, Quasi-2d fermi surface in the anomalous superconductor UTe_2, Nature Communications **15**, 223 (2024).

[13] J. F. Annett, Symmetry of the order parameter for high-temperature superconductivity, Advances in Physics **39**, 83 (1990).

[14] D. Aoki, H. Sakai, P. Opletal, Y. Tokiwa, J. Ishizuka, Y. Yanase, H. Harima, A. Nakamura, D. Li, Y. Homma, Y. Shimizu, G. Knebel, J. Flouquet, and Y. Haga, First observation of the de Haas–van Alphen Effect and Fermi surfaces in the unconventional superconductor UTe_2, Journal of the Physical Society of Japan **91**, 083704 (2022).

[15] L. Miao, S. Liu, Y. Xu, E. C. Kotta, C.-J. Kang, S. Ran, J. Paglione, G. Kotliar, N. P. Butch, J. D. Denlinger, and L. A. Wray, Low Energy Band Structure and Symmetries of UTe 2 from Angle-Resolved Photoemission Spectroscopy, Physical Review Letters **124**, 10.1103/PhysRevLett.124.076401 (2020).

[16] K. Ushida, T. Yanagisawa, R. Hibino, M. Matsuda, H. Hidaka, H. Amitsuka, G. Knebel, J. Flouquet, and D. Aoki, Lattice instability of UTe_2 studied by ultrasonic measurements, JPS Conference Proceedings **38**, 011021 (2023).